

# Interface Engineering of High-Performance Perovskite Photodetectors Based on PVP/SnO<sub>2</sub> Electron Transport Layer

Ye Wang,<sup>†,‡</sup> Xingwang Zhang,<sup>\*,†,‡,§</sup> Qi Jiang,<sup>†,‡</sup> Heng Liu,<sup>†,‡</sup> Denggui Wang,<sup>†,‡</sup> Junhua Meng,<sup>†,‡</sup> Jingbi You,<sup>†,‡</sup> and Zhigang Yin<sup>†,‡</sup>

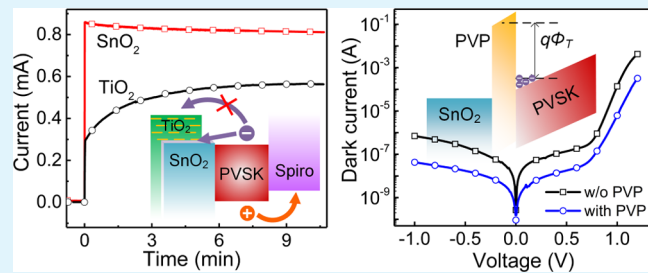
<sup>†</sup>Key Lab of Semiconductor Materials Science, Institute of Semiconductors, Chinese Academy of Sciences, Beijing 100083, P. R. China

<sup>‡</sup>College of Materials Science and Opto-Electronic Technology, University of Chinese Academy of Sciences, Beijing 100049, P. R. China

## Supporting Information

**ABSTRACT:** Hybrid organic–inorganic perovskites have attracted intensive interest as active materials for high-performance photodetectors. However, studies on the electron transport layer (ETL) and its influence on the response time of photodetectors remain limited. Herein, we compare the performances of perovskite photodetectors with TiO<sub>2</sub> and SnO<sub>2</sub> ETLs, especially on the response time. Both photodetectors exhibit a high on/off current ratio of 10<sup>5</sup>, a large detectivity around 10<sup>12</sup> Jones, and a linear dynamic range over 80 dB. The SnO<sub>2</sub>-based perovskite photodiodes show ultrahigh response rates of 3 and 6  $\mu$ s for the rise and decay times, respectively. However, photodetectors with TiO<sub>2</sub> ETLs have low responsivity and long response time at low driving voltage, which is attributed to the electron extraction barrier at the TiO<sub>2</sub>/perovskite interface and the charge traps in the TiO<sub>2</sub> layer. Furthermore, the dark current of SnO<sub>2</sub>-based perovskite photodiodes is effectively suppressed by inserting a poly(vinylpyrrolidone) interlayer, and then the on/off current ratio increases to 1.2  $\times$  10<sup>6</sup>, corresponding to an improvement of 1 order of magnitude. Such low-cost, solution-processable perovskite photodetectors with high performance show promising potential for future optoelectronic applications.

**KEYWORDS:** perovskite, photodetectors, electron transport layer, response time, dark current



## INTRODUCTION

Metal halide perovskites with an ABX<sub>3</sub> structure have attracted great attention as promising optoelectronic materials due to their unique optical and electronic properties, such as direct band gap with large absorption coefficient, ultrafast charge generation, high and microsecond-long balanced mobilities, and slow recombination.<sup>1,2</sup> Especially in the photovoltaic field, rapid progress of perovskite solar cells has been witnessed by the rocketing power conversion efficiency (PCE) rising from 3.8 to 22.1% in the past few years.<sup>3,4</sup> Besides solar cells, there have been some pioneering studies on fabricating perovskite-based photodetectors, revealing their excellent performances.<sup>5–18</sup>

Generally, perovskite-based photodetectors can be classified into two types according to the device architecture: lateral structure (photoconductors) and vertical structure (photodiodes).<sup>18–20</sup> Recently, perovskite photodetectors using a wide range of materials, including thin films, nanowires, microplates, and single crystals, have been reported.<sup>18–21</sup> In most works, the lateral structure, which employs two identical coplanar electrodes on a perovskite layer, was adopted for its fabrication simplicity. The major limitation of photoconductor devices is their long response times. In a photodiode, photoexcited electron–hole pairs are separated by the inner electric fields,

which makes it operable at zero bias without consuming external power. Furthermore, the distance between the two electrodes can be easily reduced to hundreds of nanometers by controlling the thickness of the perovskite absorption layer. Thus, photodiodes have shorter response times and lower noise than photoconductors.<sup>18,19</sup>

Similar to perovskite solar cells, perovskite photodiodes (PPDs) usually take a sandwich structure, in which a perovskite film is sandwiched between an electron transport layer (ETL) and a hole transport layer. For perovskite solar cells, developing new electron transport materials and modifying the interlayer have been demonstrated to be an effective approach to improve device efficiency and stability. It might be thought that the ETL could also be a crucial factor in determining the performance of PPDs. However, the effects of ETL on the performance of PPDs were rarely studied. In most works, the commonly used electron transport materials in perovskite solar cells, such as TiO<sub>2</sub>, C<sub>60</sub>, [6,6]-phenyl-C<sub>61</sub> butyric acid methyl ester (PCBM), and poly[(9,9-bis(3'-(N,N-dimethylamino)propyl)-2,7-flu-

Received: December 5, 2017

Accepted: January 29, 2018

Published: January 29, 2018

rene)-*alt*-2,7-(9,9-dioctylfluorene)] (PFN), were directly used as ETLs in PPDs. Recently, adopting composite ETLs, such as PFN/PCBM,<sup>6</sup> Al<sub>2</sub>O<sub>3</sub>/PCBM,<sup>7</sup> PCBM/C<sub>60</sub>,<sup>8</sup> PCBM/TiO<sub>2</sub>,<sup>22</sup> and PCBM/poly(methyl methacrylate),<sup>23</sup> has shown, in many instances, enhancement of device performance. Using a conjugated polymer PFN as the hole-blocking layer on the top of PCBM ETL in an inverted-structure photodiode, Dou et al. reduced the dark current density and achieved a very high detectivity of 10<sup>14</sup> Jones.<sup>6</sup> Lin et al. utilized relatively thick PCBM/C<sub>60</sub> ETLs to manipulate the device electro-optics, from whence they achieved control over junction capacitance, dark current, and frequency response without compromising the linear dynamic range (LDR).<sup>8</sup> As aforementioned, many studies have been reported on the suppression of dark current densities by modifying ETLs due to improving hole-blocking ability or passivating the interface defects. Nevertheless, there is no report on the influence of ETLs on the response time of PPDs. Further improvements in the performance of PPDs are also expected by designing and optimizing ETLs to achieve large responsivity, high specific detectivity, and short response time.

As mentioned previously, a series of efficient ETLs have been developed to improve the performances of perovskite solar cells. Among them, solution-based TiO<sub>2</sub> is the most commonly used electron transport material because it has specific energy level, resulting in excellent electron-transporting and hole-blocking characteristics. In addition to TiO<sub>2</sub>, SnO<sub>2</sub> has been recently shown to be a more efficient electron transport material in perovskite solar cells.<sup>24–28</sup> SnO<sub>2</sub> has a deeper conduction band and higher electron mobility compared to traditional TiO<sub>2</sub>, which can enhance charge transfer from perovskite to electron transport layers.<sup>28</sup> In this study, we compared the performances of PPDs with different ETLs, especially on the response time. Two commonly used ETLs in perovskite solar cells, i.e., TiO<sub>2</sub> and SnO<sub>2</sub>, were adopted for fabricating PPDs. Both PPDs exhibit a high on/off current ratio of 10<sup>5</sup>, a large detectivity around 10<sup>12</sup> Jones, and an LDR of over 80 dB. We found that the photodetectors with TiO<sub>2</sub> ETLs had low responsivity and long response time at low driving voltage, which is similar with the “light-soaking” effect in perovskite solar cells. The poor performance of TiO<sub>2</sub>-based PPDs under low driving voltages is attributed to the presence of electron extraction barrier at the TiO<sub>2</sub>/perovskite interface and the charge traps in the TiO<sub>2</sub> layer. Unlike the TiO<sub>2</sub>-based devices, SnO<sub>2</sub>-based PPDs show an ultrahigh response rate. Moreover, the dark current is effectively suppressed by inserting a poly(vinylpyrrolidone) (PVP) interlayer as an interfacial layer, and then the on/off current ratio increases to 1.2 × 10<sup>6</sup>, corresponding to an improvement of 1 order of magnitude.

## RESULTS AND DISCUSSION

The device structure of perovskite photodetectors used in this work has the following architecture: indium tin oxide (ITO)/ETL (SnO<sub>2</sub> or TiO<sub>2</sub>)/perovskite/2,2',7,7'-tetrakis(*N,N*-di-*p*-methoxyphenylamine)-9,9'-spirobifluorene (Spiro-MeOTAD)/Au, as schematically shown in Figure 1a. On top of the ITO-coated glass (as cathode), the SnO<sub>2</sub> or TiO<sub>2</sub> nanoparticle films were spin-coated and then low-temperature-annealed. The perovskite layer was prepared by the two-step method and sandwiched between the ETL and the spin-coated Spiro-MeOTAD layer. Finally, Au top electrodes (as anode) were thermally evaporated through a shadow mask. Figures 1b and S1 show the typical cross-sectional scanning electron microscopy (SEM) images of PPDs based on SnO<sub>2</sub> and TiO<sub>2</sub>

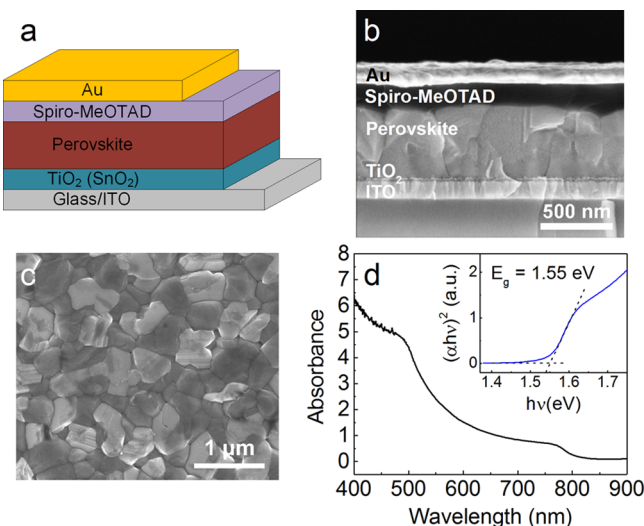


**Figure 1.** (a) Schematic diagram of the device structure of the perovskite photodetector. (b) Cross-sectional SEM image of the completed TiO<sub>2</sub>-based PPD. (c) SEM image of the fabricated (FAPbI<sub>3</sub>)<sub>1-x</sub>(MAPbBr<sub>3</sub>)<sub>x</sub> film on top of the ITO/TiO<sub>2</sub> layer. (d) UV-visible (vis) absorption spectrum of the perovskite film on a quartz substrate (the inset shows optical band gap (1.55 eV) analysis of perovskite from (d)).

ETLs, respectively, and each of the component layers can be easily distinguished. The thicknesses of TiO<sub>2</sub>, perovskite, Spiro-MeOTAD, and Au layer are 30, 500, 150, and 130 nm, respectively. X-ray diffraction (XRD) peaks for SnO<sub>2</sub> and TiO<sub>2</sub> nanoparticle films are indexable to the anatase TiO<sub>2</sub> structure and the tetragonal SnO<sub>2</sub> structure (Figure S2),<sup>29</sup> respectively, indicating the formation of pure TiO<sub>2</sub> and SnO<sub>2</sub> crystals. The average crystalline sizes of the nanoparticles were estimated by the Debye–Scherrer equation to be 2.5 nm for TiO<sub>2</sub> and 4.6 nm for SnO<sub>2</sub>. The thicknesses of SnO<sub>2</sub> and TiO<sub>2</sub> layers have been optimized, and the ETLs should fully cover the ITO substrate, but they must not be so thick as to introduce a high series resistance.

It has been reported that a small amount of MAPbBr<sub>3</sub> added into FAPbI<sub>3</sub> is favorable for improving perovskite phase stabilization.<sup>30</sup> In this work, a mixture of perovskite layer (FAPbI<sub>3</sub>)<sub>1-x</sub>(MAPbBr<sub>3</sub>)<sub>x</sub> was selected, and the composition of MAPbBr<sub>3</sub> was about 3%. Figure 1c presents the surface morphology of the fabricated (FAPbI<sub>3</sub>)<sub>1-x</sub>(MAPbBr<sub>3</sub>)<sub>x</sub> film on top of the ITO/TiO<sub>2</sub> layer. The perovskite film shows a uniform and pinhole-free surface morphology as well as well-developed grains with sizes of a few hundred nanometers. In addition, some white particles were formed on the surface of the perovskite film, which was confirmed to be PbI<sub>2</sub> by the corresponding XRD pattern (Figure S3), due to partial decomposition of the FAPbI<sub>3</sub> layer during annealing.<sup>28</sup> Previous works indicated that PbI<sub>2</sub> could passivate the defects and reduce recombination, and the perovskite film with appropriate excess PbI<sub>2</sub> has been shown to improve device performance.<sup>28,31,32</sup> The XRD (Figure S3) and SEM (Figure S4) results indicate that different substrates (TiO<sub>2</sub> and SnO<sub>2</sub>) have little influence on the morphology and quality of perovskite layers. Moreover, the strong and broad absorption in the UV and visible-light ranges reveals that the (FAPbI<sub>3</sub>)<sub>0.97</sub>(MAPbBr<sub>3</sub>)<sub>0.03</sub> perovskite layer is a good light absorber, as shown in Figure 1d. A very sharp absorption edge is a strong indication for a direct band

semiconductor,<sup>33</sup> the optical band gap of (FAPbI<sub>3</sub>)<sub>0.97</sub>(MAPbBr<sub>3</sub>)<sub>0.03</sub> is estimated to be 1.55 eV (inset of Figure 1d), which is consistent with the previously reported values.<sup>26,30,34</sup>

Figure 2a shows the current density–voltage ( $J$ – $V$ ) curves of the SnO<sub>2</sub>- and TiO<sub>2</sub>-based PPDs measured in the dark and

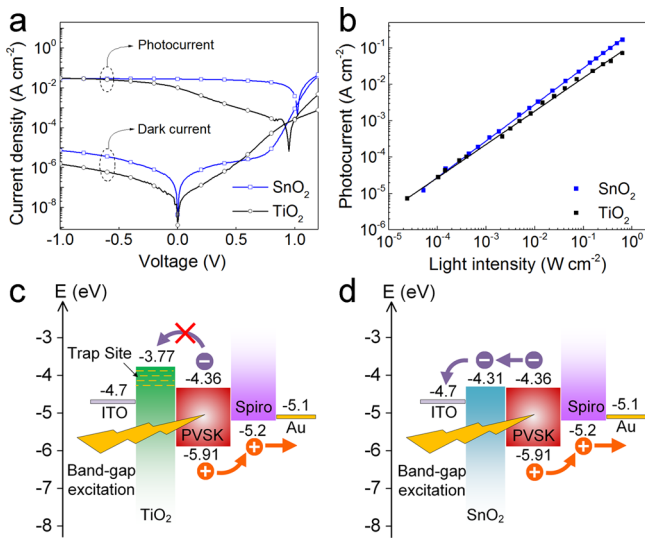


**Figure 2.** (a)  $J$ – $V$  curves of the SnO<sub>2</sub>- and TiO<sub>2</sub>-based PPDs measured in the dark and under 450 nm laser irradiation with a light density of 100 mW cm<sup>-2</sup>. (b) Linear dynamic range of TiO<sub>2</sub>- and SnO<sub>2</sub>-based PPDs. Energy band diagram at 0 V bias under illumination of (c) TiO<sub>2</sub>-based and (d) SnO<sub>2</sub>-based PPDs.

under 450 nm laser irradiation with a light density of 100 mW cm<sup>-2</sup>. As extracted from Figure 2a, dark currents of the SnO<sub>2</sub>- and TiO<sub>2</sub>-based PPDs are  $2.8 \times 10^{-6}$  and  $4.6 \times 10^{-7}$  A cm<sup>-2</sup> under a reverse bias of −0.5 V, respectively. The slightly higher

dark current for the SnO<sub>2</sub>-based PPD is attributed to the higher conductivity of SnO<sub>2</sub> than TiO<sub>2</sub> because the mobility of the SnO<sub>2</sub> film ( $1.9 \times 10^{-3}$  cm<sup>2</sup> V<sup>-1</sup> s) is 2 orders of magnitude higher than that of TiO<sub>2</sub> ( $3.3 \times 10^{-5}$  cm<sup>2</sup> V<sup>-1</sup> s).<sup>28</sup> The photocurrent keeps almost a constant value of  $\sim 30$  mA cm<sup>-2</sup> when the reverse bias decreases from −1.0 to 0 V for the SnO<sub>2</sub>-based PPD. In contrast to the SnO<sub>2</sub>-based PPD, the TiO<sub>2</sub>-based device exhibits bias-dependent photocurrent, which keeps at the same level as the SnO<sub>2</sub>-based device under the larger reverse bias. Nevertheless, the photocurrent decreases obviously when the reverse bias is lower than −0.6 V. The different photocurrent–voltage characteristics lead to a distinct difference in the light on/off ratio. The on/off ratios were determined to be  $4.1 \times 10^3$  and  $2.0 \times 10^4$  under −1.0 V for the SnO<sub>2</sub>- and TiO<sub>2</sub>-based PPDs, respectively. At a low reverse bias of −0.05 V, the on/off ratio improves to the same level of  $2.0 \times 10^5$  for both PPDs. As one of the most important parameters, the specific detectivity ( $D^*$ ) characterizes how weak light it can detect. When the dark current is dominated by short noise,  $D^*$  can be expressed as

$$D^* = \frac{J_{ph}/L_{light}}{(2qJ_d)^{1/2}} \quad (1)$$

where  $J_{ph}$  is the photocurrent,  $L_{light}$  is the incident light intensity,  $J_d$  is the dark current, and  $q$  is the elementary charge. The specific detectivity at 450 nm was then calculated to be about  $1.2 \times 10^{12}$  Jones (Jones = cm Hz<sup>1/2</sup> W<sup>-1</sup>) under −0.05 V for both PPDs. This value is comparable to the commercial Si photodiode at the same wavelength,<sup>35</sup> demonstrating its potential application in weak visible-light sensing. Another figure of merit of photodetectors is the LDR, which represents the light intensity range in which the responsivity of the photodetector keeps constant. Figure 2b shows that the photocurrent increases linearly with increasing light intensity

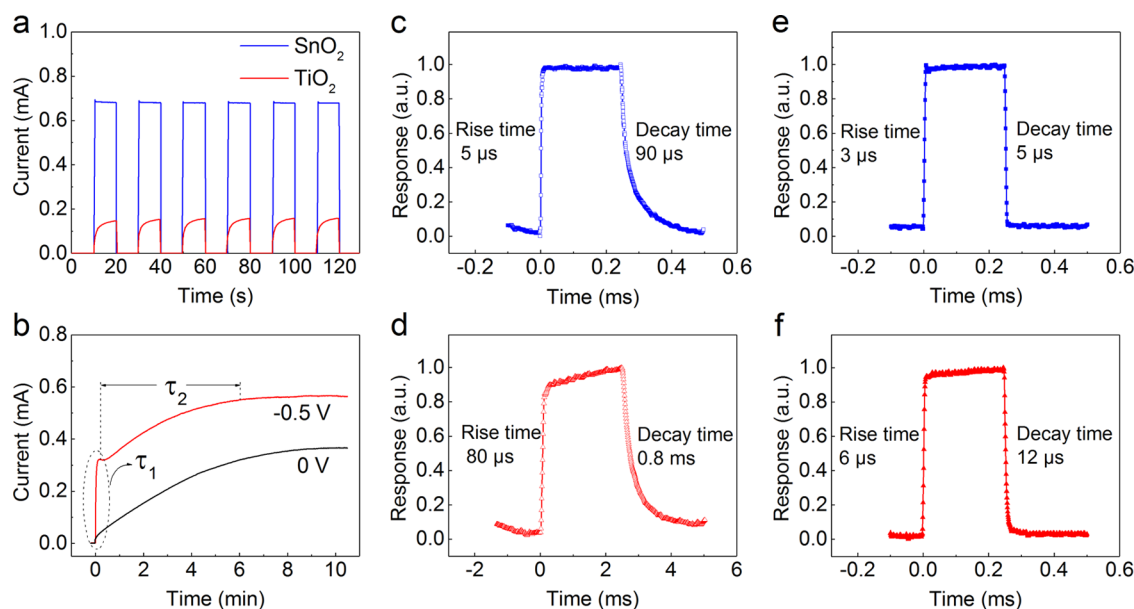


**Figure 3.** (a)  $I$ – $t$  curves of the SnO<sub>2</sub>- and TiO<sub>2</sub>-based PPDs at 0 V bias under 450 nm irradiation with a light density of 60 mW cm<sup>-2</sup>. (b)  $I$ – $t$  curves of the TiO<sub>2</sub>-based PPD under 450 nm laser irradiation at different bias voltages after a single switch-on operation. The rise time can be divided into two components.  $\tau_1$  is a transient response with a very short time constant, whereas  $\tau_2$  shows a time constant of around 6 min. (c–f) Normalized high-resolution photoresponse of the (c, e) SnO<sub>2</sub>-based PPDs and (d, f) TiO<sub>2</sub>-based PPDs at (c, d) 0 V and (e, f) −0.5 V reverse bias for rise and decay times.

across greater than 4 decades of laser intensity, corresponding to an LDR exceeding 80 dB.

The difference in photoresponse for the photodetectors with different ETLs can be understood from their energy band diagram at 0 V bias under illumination, as shown in Figure 2c,d, in which the data of energy band levels are taken from the previous works.<sup>6,28,36,37</sup> In view of the line-up presented in Figure 2c,d, there appears to be an energy barrier of 0.59 eV between the conduction band minimum (CBM) of (FAPbI<sub>3</sub>)<sub>0.97</sub>(MAPbBr<sub>3</sub>)<sub>0.03</sub> and TiO<sub>2</sub>, whereas there is almost no barrier in the SnO<sub>2</sub>/perovskite case. Thus, photogenerated electrons hardly move from the perovskite layer to the ITO through the barrier in the TiO<sub>2</sub>-based PPDs, leading to lower photocurrents at the lower reverse bias. When the reverse bias is higher than the energy barrier of 0.59 V, the driving force imposed onto the photogenerated electrons is enough to overcome the energy barrier between TiO<sub>2</sub> and perovskite, thereby resulting in an almost same photocurrent as the SnO<sub>2</sub>-based device.

To explore the response characteristics, the current–time ( $I-t$ ) curves were measured at 0 V bias under 450 nm laser irradiation with a light density of 60 mW cm<sup>-2</sup> for both PPDs, as shown in Figure 3a. The current in the dark and under illumination was controlled by a light shutter. The photocurrent of the SnO<sub>2</sub>-based PPD is higher than that of the TiO<sub>2</sub>-based device, which is consistent with the results in Figure 2a. The on/off switching behavior for both PPDs is preserved over multiple cycles, indicating the robustness and reproducibility of both photodetectors. In notable contrast, however, the photocurrent sharply increases for the SnO<sub>2</sub>-based PPD after the laser is turned on, whereas it slowly rises with time for the TiO<sub>2</sub>-based device. Similar temporal photoresponse characteristics were also observed for both PPDs under -0.5 V reverse bias (Figure S5). To further explore the temporal photoresponse, the  $I-t$  curves of the TiO<sub>2</sub>- and SnO<sub>2</sub>-based PPDs were measured under 450 nm laser irradiation after a single switch-on operation, as shown in Figures 3b and S6, respectively. Obviously, the rise time of the TiO<sub>2</sub>-based PPD can be divided into two components. The first component ( $\tau_1$ ) is a transient response with a very short time constant, whereas the second component ( $\tau_2$ ) shows a time constant of around 6 min. Unlike the TiO<sub>2</sub>-based PPDs, the SnO<sub>2</sub>-based detectors exhibit a transient response without the slow component (Figure S6). The phenomenon of double-exponential rise indicates the existence of two mechanisms, probably related to intrinsic photoresponse and light-soaking effect, which will be discussed in detailed later.

To obtain a precise value of  $\tau_1$ , the  $I-t$  curves of the device were measured using a 450 nm continuous laser, which was switched on and off by a chopper. The rise time and decay time are defined as the time rise to 90% of the maximum photocurrent from the dark current and recovery to 10% of the maximum photocurrent, respectively. As shown in Figure 3c, the rise time and decay time of the SnO<sub>2</sub>-based photodetector at 0 V are determined to be 5 and 90  $\mu$ s, respectively. In contrast, the on/off switching of the TiO<sub>2</sub>-based PPDs at 0 V is obviously slower than that of the SnO<sub>2</sub>-based device, and it shows an 80  $\mu$ s rise time and a 0.8 ms decay time (Figure 3d). The higher response speed for the SnO<sub>2</sub>-based device is attributed to a better match of energy level between SnO<sub>2</sub> and perovskite. The rise time depends on the collection of photogenerated carriers, and electrons in the perovskite layer can be efficiently transported to the SnO<sub>2</sub> layer because the

CBM of SnO<sub>2</sub> is very close to that of perovskite. On the contrary, electrons hardly move from the perovskite layer to TiO<sub>2</sub> because of an energy barrier of 0.59 eV. Thus, the rise time of the SnO<sub>2</sub>-based detector is shorter than that of the TiO<sub>2</sub>-based device. Furthermore, in all devices, the decay time is shorter than the rise time, indicating the slow recombination of holes and electrons in the perovskite layer. It is known that the photocurrent decay time of detector is related to the carrier recombination time. As shown in Figure 2c, for both devices, holes can be efficiently and rapidly transported to the Au anode because of the lower valence band maximum of Spiro-MeOTAD compared to the perovskite. However, there appears to be a small energy barrier of 0.05 eV between the CBM of SnO<sub>2</sub> and perovskite, the electron and hole fluxes cannot be balanced, and the electrons are accumulated at traps in the SnO<sub>2</sub>/perovskite layer under 0 V bias. Consequently, the recombination of the photogenerated electron–hole pairs in the perovskite layer is reduced, resulting in increased carrier lifetime. This effect (i.e., accumulation of photogenerated electrons at the TiO<sub>2</sub>/perovskite interface) is more dominant for the TiO<sub>2</sub>-based device because of the much higher energy barrier of 0.59 eV. As a result, the decay process becomes limited by the poor recombination cross section.

When the PPDs are operated under a reverse bias of -0.5 V, both rise and decay times are significantly reduced (Figure 3e,f). The extracted rise and decay times are 3 and 6  $\mu$ s for the SnO<sub>2</sub>-based PPD at -0.5 V, respectively, which are comparable to the best reported values for perovskite photodetectors.<sup>7,8</sup> In addition, unlike at 0 V bias, the rise time and decay time (6 and 12  $\mu$ s, respectively) of the TiO<sub>2</sub>-based PPD are closer than those of the SnO<sub>2</sub>-based device (3 and 5  $\mu$ s, respectively). In the presence of reverse bias, the driving force imposed onto the photogenerated electrons is enough to overcome the energy barrier between ETL and perovskite. Therefore, both electrons and holes can be efficiently and rapidly extracted to respective electrodes and the decay time is close to the rise time for both PPDs.

The temporal photoresponse of PPDs was also investigated under forward bias to investigate the origin of long component rise time. When the device is biased at zero bias or forward bias, it is in photovoltaic mode and operated as a solar cell. The  $J-V$  curves of the TiO<sub>2</sub>-based PPD with different light-irradiation times are shown in Figure 4a. The TiO<sub>2</sub>-based device exhibits S-shaped  $J-V$  curves in the initial illumination with lower PCE and fill factor. With increasing irradiation time, the device metrics gradually recover and finally reach a saturated state after 8 min irradiation. This process was previously known as the “light-soaking” issue in polymer and perovskite solar cells.<sup>38–41</sup> By contrast, the SnO<sub>2</sub>-based detector has reproducible and stable  $J-V$  characteristics during the initial  $J-V$  sweep and upon different irradiation times (Figure S7), demonstrating the absence of a light-soaking problem. Trap-filling in TiO<sub>2</sub> by photogenerated charges, leading to an increased conductivity of the TiO<sub>2</sub> layer, has been proposed to be the underlying reason.<sup>38,39</sup> One way to overcome the light-soaking problem is to chemically dope TiO<sub>2</sub> with other elements, which can significantly reduce its work function. Furthermore, the light-soaking effects are more negative for photodetectors than for solar cells because solar cells usually work under steady-state illumination, whereas a fast response for illumination is required for most photodetectors.

To reveal the possible effects of ETLs on the photoresponse of devices, the  $I-V$  characteristics of both TiO<sub>2</sub> and SnO<sub>2</sub> thin

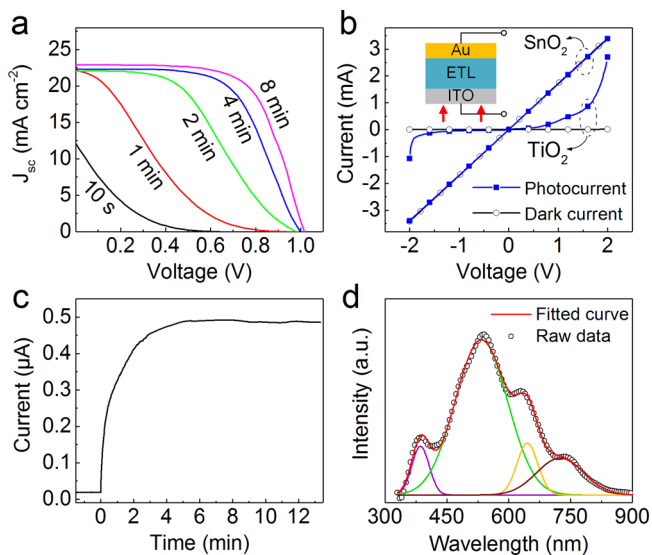


**Figure 4.** (a)  $J$ – $V$  curves of the  $\text{TiO}_2$ -based PPD operated as a solar cell under a simulated AM1.5G spectrum with different light-irradiation times. (b)  $I$ – $V$  characteristics of  $\text{TiO}_2$  and  $\text{SnO}_2$  thin films with device structure of ITO/metal oxides/Au with and without 450 nm laser illumination. The inset shows the device structure. (c) Temporal photocurrent response of the  $\text{TiO}_2$  film under 450 nm laser illumination. (d) Photoluminescence (PL) spectrum of the  $\text{TiO}_2$  film at room temperature and its four Gaussian fit peaks.

films with device structure of ITO/metal oxides/Au were measured with and without light illumination, as shown in Figure 4b. The dark current of the  $\text{SnO}_2$  film is much higher than that of the  $\text{TiO}_2$  film, confirming the higher conductivity of the  $\text{SnO}_2$  layer. More importantly, the photocurrent of the  $\text{SnO}_2$  film is very close to its dark current, whereas the  $\text{TiO}_2$  film shows a drastic increase in current after light illumination. This result implies the presence of a photoconductivity effect in the  $\text{TiO}_2$  film. To further evaluate the photoconductivity effect, Figure 4c shows the temporal photocurrent response of the  $\text{TiO}_2$  film. Upon light illumination, the photocurrent exponentially increases with irradiation time with a time constant of  $\sim 4$  min, which is very close to the long component rise time  $\tau_2$  and the light-soaking time for the  $\text{TiO}_2$ -based PPDs, implying the same mechanism. Therefore, we propose that the long component rise time for the  $\text{TiO}_2$ -based detector, as well as the light-soaking effect, is attributed to the photoconductivity effect of the  $\text{TiO}_2$  layer.

To fully reveal the underlying mechanism of long component rise time, we measured the photoluminescence (PL) spectrum of  $\text{TiO}_2$  film at room temperature. The original PL spectrum of  $\text{TiO}_2$  and its four Gaussian fitting peaks are illustrated in Figure 4d. The 386 nm peak is originated from the transition of electrons from the conduction band to the valence band, according to the electronic structure of anatase (3.2 eV). The broad peak at 534 nm is associated with the oxygen vacancies losing one electron ( $\text{F}^+$  center).<sup>42,43</sup> The PL peaks at 645 and 724 nm are related to the formation of  $\text{Ti}^{3+}$  ions and the associated defect states.<sup>44</sup> The defect-related emission in the visible region is very strong compared to the UV emission, inferring the high defect density inside the  $\text{TiO}_2$  film. We propose that the presence of a large number of defects in  $\text{TiO}_2$  is responsible for the long component rise time  $\tau_2$  (as well as the light-soaking effect) observed in the  $\text{TiO}_2$ -based detector. As demonstrated in Figure 4c, the conductivity of  $\text{TiO}_2$  is sensitive to light exposure because illumination can lead to the direct excitation of electrons from the valence band to the conduction band (or from the valence band to the defect states). Upon light illumination, the initially excited electrons must fill the defect states that are present in the forbidden band of  $\text{TiO}_2$  and then the photoconductivity increased gradually under continuous illumination and saturated when all of the defect states are filled. Increasing photoconductivity of  $\text{TiO}_2$  reduces the serial resistance of the  $\text{TiO}_2$ -based PPDs, resulting in the observed long component rise time  $\tau_2$ .

The above results suggest that the performance of  $\text{SnO}_2$ -based PPDs is better than that of  $\text{TiO}_2$ -based devices owing to a better match of energy level between  $\text{SnO}_2$  and perovskite compared to  $\text{TiO}_2$ . However, the dark current of  $\text{SnO}_2$ -based PPD is relatively high due to the higher conductivity of the  $\text{SnO}_2$  layer. Previous works have demonstrated that the dark current of PPDs could be significantly suppressed by adding an interlayer or through interfacial engineering.<sup>6–8,22</sup> In this work, a thin poly(vinylpyrrolidone) (PVP) interlayer, which has a larger optical band gap than  $\text{SnO}_2$ , was inserted between  $\text{SnO}_2$  ETL and perovskite layer to suppress the dark current. The thickness of the PVP layer varied from 2.1 to 7.8 nm by controlling the concentration of the precursor solution (Figure S8). As demonstrated in Figures S3 and S4, the thin PVP interlayer has little effect on the morphology and quality of the subsequent perovskite layer. The optimum thickness of the PVP interlayer was determined to be  $\sim 3.2$  nm (Figure S9). Figure 5a shows the dark current and photocurrent density curves (under 450 nm laser irradiation with a light density of  $100 \text{ mW cm}^{-2}$ ) of the  $\text{SnO}_2$ -based PPDs with and without a 3.2 nm PVP interlayer. (b) EQE spectra and spectral responsivity ( $R_\lambda$ ) of the  $\text{SnO}_2$ -based PPDs with and without a 3.2 nm PVP interlayer. (c, d) Schematic energy band diagram of the  $\text{SnO}_2$ -based PPD with a thin PVP interlayer (c) in dark and (d) under light illumination.

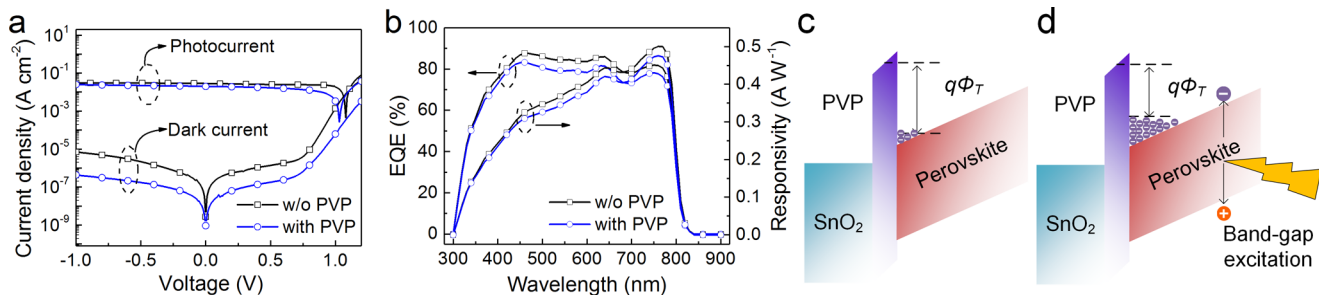


**Figure 5.** (a) Dark current and photocurrent density curves (under 450 nm laser irradiation with a light density of  $100 \text{ mW cm}^{-2}$ ) of the  $\text{SnO}_2$ -based PPDs with and without a 3.2 nm PVP interlayer. (b) EQE spectra and spectral responsivity ( $R_\lambda$ ) of the  $\text{SnO}_2$ -based PPDs with and without a 3.2 nm PVP interlayer. (c, d) Schematic energy band diagram of the  $\text{SnO}_2$ -based PPD with a thin PVP interlayer (c) in dark and (d) under light illumination.

100 mW/cm<sup>2</sup>) of the SnO<sub>2</sub>-based PPD with and without a 3.2 nm PVP interlayer under the bias ranging from −1.0 to 1.2 V, respectively. As extracted from Figure 5a, after introducing the PVP interlayer, the dark current greatly reduces from  $1.6 \times 10^{-7}$  to  $1.8 \times 10^{-8}$  A cm<sup>−2</sup> under a reverse bias of −0.05 V, whereas the photocurrent is only slightly decreased from 28.5 to 20.2 mA cm<sup>−2</sup>. Then, the light on/off ratios were determined to be  $1.2 \times 10^6$  and  $1.8 \times 10^5$  for the SnO<sub>2</sub>-based PPDs with and without the PVP interlayer, respectively. Notably, by introducing the PVP interlayer, the on/off ratio is enhanced by approximately 1 order of magnitude. The external quantum efficiency (EQE) and spectral responsivity ( $R_\lambda$ ) of the photodetector with and without PVP interlayer at different wavelengths are shown in Figure 5b, respectively. Both devices exhibit high EQEs (75–85%) in the wavelength range of 400–760 nm and hence they are suitable for visible-light broad-band photodetection. After adding the PVP interlayer, both EQE and  $R_\lambda$  drop little, which is consistent with the slight reduction of photocurrent for the device with PVP layer. Besides, the photoswitching behavior (Figure S10) and the LDR (Figure S11) of the SnO<sub>2</sub>-based PPD with the PVP interlayer show similar features compared to its counterpart without the PVP interlayer.

These results demonstrate that the PVP interlayer can effectively suppress the dark current of perovskite photodetectors and that it has little effect on the other device performance, which can be understood on the basis of the energy diagram shown in Figure 5c,d. When the PVP insulator layer is thin, the carrier transport from the perovskite film to the SnO<sub>2</sub> layer is controlled by direct tunneling. The introduction of PVP interlayer will incur an additional tunneling probability factor for the device current, which can be described by eq 2<sup>45</sup>

$$J \propto T_t \approx \exp(-\alpha_T d \sqrt{q\phi_T}) \quad (2)$$

where  $\alpha_T = 2\sqrt{2qm^*/\hbar}$  approaches unity if the effective mass in the insulator equals the free electron mass,  $d$  is the thickness of PVP layer,  $q$  is the elementary charge, and  $\phi_T$  is the tunnel barrier height. It is obvious that after inserting the PVP interlayer the additional tunneling probability factor  $T_t$  will significantly reduce the dark current density because of the higher  $\phi_T$ . Upon illumination, with a photoenergy larger than that of the semiconductor band gap, the perovskite film absorbs photons to generate a large number of electron–hole pairs. These photogenerated electrons give rise to an increase in electron-filling level in the conduction band of perovskite, resulting in a reduction of the tunnel barrier height  $\phi_T$ , as shown in Figure 5d. As the tunnel barrier height decreases, the tunneling probability factor  $T_t$  increases and consequently the photocurrent recovers its initial level of the counterpart without the PVP interlayer. In other words, the increased carrier density in the perovskite film upon illumination lowers the effective barrier height, leading to the easier carrier tunneling and transport and thus to an amelioration of negative effect of the PVP interlayer in the photocurrent.

## CONCLUSIONS

In summary, the PPDs based on SnO<sub>2</sub> and TiO<sub>2</sub> ETLs were fabricated via a facile and low-cost solution-processing strategy and their performances were compared. Both PPDs exhibit a high on/off current ratio of  $10^5$ , a large detectivity of more than  $10^{12}$  Jones, and a linear dynamic range of over 80 dB. Because

of the electron extraction barrier at the TiO<sub>2</sub>/perovskite interface and charge traps in the TiO<sub>2</sub> layer, the TiO<sub>2</sub>-based PPDs exhibit worse performance under low driving voltage, such as a low responsivity and a long response time. Especially, the temporal response of TiO<sub>2</sub>-based PPDs indicates two different decay times on the order of 80 μs and 0.8 ms at 0 V and the photoconductivity effect of the TiO<sub>2</sub> layer is responsible for the observed long component rise time. Furthermore, the SnO<sub>2</sub>-based PPDs show an ultrahigh response rate of 3 μs for the rise and 6 μs for the decay times at −0.5 V. The dark current of SnO<sub>2</sub>-based PPDs is suppressed effectively by introducing a PVP interlayer, and the on/off current ratio is increased by 1 order of magnitude, whereas the other device performance keeps almost unchanged. This work inspires the development of cheap and high-performance perovskite-based photodetectors.

## EXPERIMENTAL SECTION

**Materials.** SnO<sub>2</sub> colloid precursor was purchased from Alfa Aesar (tin(IV) oxide, 15% in H<sub>2</sub>O colloidal dispersion). TiO<sub>2</sub> nanoparticles were prepared by the method mentioned in ref 28. The final TiO<sub>2</sub> nanoparticles were dispersed in ethanol to make a suspension with a concentration of 6 mg mL<sup>−1</sup>. TiAcAc was added into the solution with a final concentration of 15 μL mL<sup>−1</sup> to stabilize the as-obtained TiO<sub>2</sub> solutions. Lead iodide (PbI<sub>2</sub>) was dissolved in dimethylformamide with a concentration of 1.3 mol mL<sup>−1</sup>. The mixture solutions of FAI/MABr/MACl were prepared by dissolution of HC(NH<sub>2</sub>)<sub>2</sub>I, CH<sub>3</sub>NH<sub>3</sub>Br, and CH<sub>3</sub>NH<sub>3</sub>Cl (60:6:6 by weight in milligrams) in 1 mL isopropyl alcohol. The Spiro-OMeTAD solution was prepared by dissolving 72.3 mg of 2,2',7,7'-tetrakis(*N,N'*-di-*p*-methoxyphenylamine)-9,9'-spirobifluorene in 1 mL of chlorobenzene with 30 μL of 4-*tert*-butylpyridine and 35 μL of Li-bis(trifluoromethanesulfonyl)-imide (170 mg mL<sup>−1</sup> in acetonitrile).

**Device Fabrication.** The glass/ITO substrate with a sheet resistance of 15 Ω sq<sup>−1</sup> was sequentially washed with detergent, distilled water, acetone, and isopropyl alcohol. After drying with nitrogen, the cleaned ITO substrates were treated with UV ozone for 10 min. For SnO<sub>2</sub> films, the ITO substrate was spin-coated with a thin layer of SnO<sub>2</sub> nanoparticle (diluted to 5%) at 4000 rpm for 30 s and annealed in ambient air at 180 °C for 30 min. For TiO<sub>2</sub> films, 6 mg mL<sup>−1</sup> TiO<sub>2</sub> solution was spin-coated on ITO substrates at 2000 rpm for 30 s and annealed in ambient air at 150 °C for 30 min. After depositing the ETL, the perovskite layer was deposited in a glovebox by a two-step spin-coating method. First, 1.3 M PbI<sub>2</sub> solution was spin-coated onto the SnO<sub>2</sub> or TiO<sub>2</sub> ETL at 2500 rpm for 30 s and then annealed at 70 °C for 15 min. After the PbI<sub>2</sub> had cooled to room temperature, the mixture solution of FAI/MABr/MACl was spin-coated onto the PbI<sub>2</sub> layer at 2500 rpm for 30 s and then thermally annealed at 150 °C for 15 min under ambient condition. Next, the Spiro-OMeTAD solution was spin-coated at 2500 rpm for 30 s. Finally, the Au electrode (100 nm) was deposited on the Spiro-OMeTAD layer at a rate of 4 Å s<sup>−1</sup> via thermal evaporation using a shadow mask. For PVP interface-modified devices, after spin-coating SnO<sub>2</sub> films, 0.5 wt % PVP solution in dimethyl sulfoxide was spin-coated onto the SnO<sub>2</sub> layer at 2000 rpm for 1 min and then annealed at 150 °C for 15 min to induce cross-linking.

**Characterization.** Field emission scanning electron microscopy (FEI Nova Nano SEM-650) was used to acquire SEM images, with an electron beam accelerated at 500 V to 30 kV. X-ray diffraction (XRD) measurements were carried out using a Rigaku D/MAX-2500 diffractometer with a Cu Kα X-ray source. PL spectra of TiO<sub>2</sub> thin films on Si substrate were measured with a Raman spectrometer (Horiba Jobin Yvon LabRam HR800) at room temperature, using a continuous beam of He–Cd laser of 325 nm wavelength as the excitation source. The optical absorption spectra of the samples were acquired using a Varian Cary 5000 UV–vis spectrophotometer in double-beam mode. The PVP film thickness was measured by an ellipsometer. All of the device measurements were performed under

ambient conditions. The  $I$ – $V$  characteristics were acquired using a Keithley 2450 source meter in the dark and under illumination. A diode laser with wavelength of 450 nm was utilized as the light source, and the output power was measured using a laser power meter. The temporal photocurrent response was measured by a Tektronix TDS2012B Digital Storage Oscilloscope. The on–off illumination was switched by a mechanical chopper, and the frequency was 200 or 2000 Hz. When the PPDs were operated in solar cell mode, the  $J$ – $V$  curves were taken using a Keithley 2400 source measurement unit under a simulated AM1.5G spectrum. The EQE spectra were recorded with an Enli Tech (Taiwan) EQE measurement system.

## ■ ASSOCIATED CONTENT

### Supporting Information

The Supporting Information is available free of charge on the ACS Publications website at DOI: [10.1021/acsami.7b18511](https://doi.org/10.1021/acsami.7b18511).

SEM images, XRD patterns, UV–visible absorption spectra, and photodetector results ([PDF](#))

## ■ AUTHOR INFORMATION

### Corresponding Author

\*E-mail: [xwzhang@semi.ac.cn](mailto:xwzhang@semi.ac.cn).

### ORCID

Xingwang Zhang: [0000-0001-7873-5566](https://orcid.org/0000-0001-7873-5566)

### Notes

The authors declare no competing financial interest.

## ■ ACKNOWLEDGMENTS

This work was financially supported by the National Key Research and Development Program of China (No. 2016YFB0402301), the National Natural Science Foundation of China (Nos. 61674137, 61474105, and U1738114), and project No. 17-163-13-ZD-00100302.

## ■ REFERENCES

- (1) Jung, H. S.; Park, N.-G. Perovskite Solar Cells: From Materials to Devices. *Small* **2015**, *11*, 10–25.
- (2) Poncea, C. S.; Savenije, T. J.; Abdellah, M.; Zheng, K.; Yartsev, A.; Pascher, T.; Harlang, T.; Chabera, P.; Pullerits, T.; Stepanov, A.; Wolf, J.-P.; Sundström, V. Organometal Halide Perovskite Solar Cell Materials Rationalized: Ultrafast Charge Generation, High and Microsecond-Long Balanced Mobilities, and Slow Recombination. *J. Am. Chem. Soc.* **2014**, *136*, 5189–5192.
- (3) Kojima, A.; Teshima, K.; Shirai, Y.; Miyasaka, T. Organometal Halide Perovskites as Visible-Light Sensitizers for Photovoltaic Cells. *J. Am. Chem. Soc.* **2009**, *131*, 6050–6051.
- (4) Yang, W. S.; Park, B.-W.; Jung, E. H.; Jeon, N. J.; Kim, Y. C.; Lee, D. U.; Shin, S. S.; Seo, J.; Kim, E. K.; Noh, J. H.; Seok, S. I. Iodide Management in Formamidinium-Lead-Halide-Based Perovskite Layers for Efficient Solar Cells. *Science* **2017**, *356*, 1376–1379.
- (5) Wang, F.; Mei, J.; Wang, Y.; Zhang, L.; Zhao, H.; Zhao, D. Fast Photoconductive Responses in Organometal Halide Perovskite Photodetectors. *ACS Appl. Mater. Interfaces* **2016**, *8*, 2840–2846.
- (6) Dou, L.; Yang, Y.; You, J.; Hong, Z.; Chang, W.-H.; Li, G.; Yang, Y. Solution-Processed Hybrid Perovskite Photodetectors with High Detectivity. *Nat. Commun.* **2014**, *5*, No. 5404.
- (7) Sutherland, B. R.; Johnston, A. K.; Ip, A. H.; Xu, J.; Adinolfi, V.; Kanjanaboos, P.; Sargent, E. H. Sensitive, Fast, and Stable Perovskite Photodetectors Exploiting Interface Engineering. *ACS Photonics* **2015**, *2*, 1117–1123.
- (8) Lin, Q.; Armin, A.; Lyons, D. M.; Burn, P. L.; Meredith, P. Low Noise, IR-Blind Organohalide Perovskite Photodiodes for Visible Light Detection and Imaging. *Adv. Mater.* **2015**, *27*, 2060–2064.
- (9) Zhou, J.; Chu, Y.; Huang, J. Photodetectors Based on Two-Dimensional Layer-Structured Hybrid Lead Iodide Perovskite Semiconductors. *ACS Appl. Mater. Interfaces* **2016**, *8*, 25660–25666.
- (10) Dong, R.; Fang, Y.; Chae, J.; Dai, J.; Xiao, Z.; Dong, Q.; Yuan, Y.; Centrone, A.; Zeng, X. C.; Huang, J. High-Gain and Low-Driving-Voltage Photodetectors Based on Organolead Triiodide Perovskites. *Adv. Mater.* **2015**, *27*, 1912–1918.
- (11) Fang, Y.; Dong, Q.; Shao, Y.; Yuan, Y.; Huang, J. Highly Narrowband Perovskite Single-Crystal Photodetectors Enabled by Surface-Charge Recombination. *Nat. Photonics* **2015**, *9*, 679–686.
- (12) Shen, L.; Fang, Y.; Wang, D.; Bai, Y.; Deng, Y.; Wang, M.; Lu, Y.; Huang, J. A Self-Powered, Sub-Nanosecond-Response Solution-Processed Hybrid Perovskite Photodetector for Time-Resolved Photoluminescence-Lifetime Detection. *Adv. Mater.* **2016**, *28*, 10794–10800.
- (13) Song, J.; Xu, L.; Li, J.; Xue, J.; Dong, Y.; Li, X.; Zeng, H. Monolayer and Few-Layer All-Inorganic Perovskites as a New Family of Two-Dimensional Semiconductors for Printable Optoelectronic Devices. *Adv. Mater.* **2016**, *26*, 4861–4869.
- (14) Lu, H.; Tian, W.; Cao, F.; Ma, Y.; Gu, B.; Li, L. A Self-Powered and Stable All-Perovskite Photodetector-Solar Cell Nanosystem. *Adv. Funct. Mater.* **2016**, *26*, 1296–1302.
- (15) Yu, J.; Chen, X.; Wang, Y.; Zhou, H.; Xue, M.; Xu, Y.; Li, Z.; Ye, C.; Zhang, J.; van Aken, P. A.; Lund, P. D.; Wang, H. A High-Performance Self-Powered Broadband Photodetector Based on a  $\text{CH}_3\text{NH}_3\text{PbI}_3$  Perovskite/ZnO Nanorod Array Heterostructure. *J. Mater. Chem. C* **2016**, *4*, 7302–7308.
- (16) Liu, H.; Zhang, X.; Zhang, L.; Yin, Z.; Wang, D.; Meng, J.; Jiang, Q.; Wang, Y.; You, J. A High-Performance Photodetector Based on an Inorganic Perovskite–ZnO Heterostructure. *J. Mater. Chem. C* **2017**, *5*, 6115–6122.
- (17) Liu, Y.; Jia, R.; Wang, Y.; Hu, Z.; Zhang, Y.; Pang, T.; Zhu, Y.; Luan, S. Inhibition of Zero Drift in Perovskite-Based Photodetector Devices via [6,6]-Phenyl-C61-Butyric Acid Methyl Ester Doping. *ACS Appl. Mater. Interfaces* **2017**, *9*, 15638–15643.
- (18) Wang, H.; Kim, D. H. Perovskite-Based Photodetectors: Materials and Devices. *Chem. Soc. Rev.* **2017**, *46*, 5204–5236.
- (19) de Arquer, F. P. G.; Armin, A.; Meredith, P.; Sargent, E. H. Solution-Processed Semiconductors for Next-Generation Photodetectors. *Nat. Rev. Mater.* **2017**, *2*, No. 16100.
- (20) Zhang, Y.; Liu, J.; Wang, Z.; Xue, Y.; Ou, Q.; Polavarapu, L.; Zheng, J.; Qi, X.; Bao, Q. Synthesis, Properties, and Optical Applications of Low-Dimensional Perovskites. *Chem. Commun.* **2016**, *52*, 13637–13655.
- (21) Dong, D.; Deng, H.; Hu, C.; Song, H.; Qiao, K.; Yang, X.; Zhang, J.; Cai, F.; Tang, J.; Song, H. Bandgap Tunable  $\text{Cs}_x(\text{CH}_3\text{NH}_3)_{1-x}\text{PbI}_3$  Perovskite Nanowires by Aqueous Solution Synthesis for Optoelectronic Devices. *Nanoscale* **2017**, *9*, 1567–1574.
- (22) Liu, C.; Wang, K.; Yi, C.; Shi, X.; Du, P.; Smith, A. W.; Karim, A.; Gong, X. Ultrasensitive Solution-Processed Perovskite Hybrid Photodetectors. *J. Mater. Chem. C* **2015**, *3*, 6600–6606.
- (23) Tang, F.; Chen, Q.; Chen, L.; Ye, F.; Cai, J.; Chen, L. Mixture Interlayer for High Performance Organic–Inorganic Perovskite Photodetectors. *Appl. Phys. Lett.* **2016**, *109*, No. 123301.
- (24) Song, J.; Zheng, E.; Bian, J.; Wang, X.-F.; Tian, W.; Sanehira, Y.; Miyasaka, T. Low-Temperature  $\text{SnO}_2$ -Based Electron Selective Contact for Efficient and Stable Perovskite Solar Cells. *J. Mater. Chem. A* **2015**, *3*, 10837–10844.
- (25) Ke, W.; Fang, G.; Liu, Q.; Xiong, L.; Qin, P.; Tao, H.; Wang, J.; Lei, H.; Li, B.; Wan, J.; Yang, G.; Yan, Y. Lowerature Solution-Processed Tin Oxide as an Alternative Electron Transporting Layer for Efficient Perovskite Solar Cells. *J. Am. Chem. Soc.* **2015**, *137*, 6730–6733.
- (26) Baena, J. P. C.; Steier, L.; Tress, W.; Saliba, M.; Neutzner, S.; Matsui, T.; Giordano, F.; Jacobsson, T. J.; Kandada, A. R. S.; Zakeeruddin, S. M.; Petrozza, A.; Abate, A.; Nazeeruddin, M. K.; Grätzel, M.; Hagfeldt, A. Highly Efficient Planar Perovskite Solar Cells through Band Alignment Engineering. *Energy Environ. Sci.* **2015**, *8*, 2928–2934.

- (27) Anaraki, E. H.; Kermanpur, A.; Steier, L.; Domanski, K.; Matsui, T.; Tress, W.; Saliba, M.; Abate, A.; Grätzel, M.; Hagfeldt, A.; Correa-Baena, J.-P. Highly Efficient and Stable Planar Perovskite Solar Cells by Solution-Processed Tin Oxide. *Energy Environ. Sci.* **2016**, *9*, 3128–3134.
- (28) Jiang, Q.; Zhang, L.; Wang, H.; Yang, X.; Meng, J.; Liu, H.; Yin, Z.; Wu, J.; Zhang, X.; You, J. Enhanced Electron Extraction Using  $\text{SnO}_2$  for High-Efficiency Planar-Structure  $\text{HC}(\text{NH}_2)_2\text{PbI}_3$ -Based Perovskite Solar Cells. *Nat. Energy* **2016**, *2*, No. 16177.
- (29) Yang, S.; Yue, W.; Zhu, J.; Ren, Y.; Yang, X. Graphene-Based Mesoporous  $\text{SnO}_2$  with Enhanced Electrochemical Performance for Lithium-Ion Batteries. *Adv. Funct. Mater.* **2013**, *23*, 3570–3576.
- (30) Jeon, N. J.; Noh, J. H.; Yang, W. S.; Kim, Y. C.; Ryu, S.; Seo, J.; Seok, S. I. Compositional Engineering of Perovskite Materials for High-Performance Solar Cells. *Nature* **2015**, *517*, 476–480.
- (31) Kim, Y. C.; Jeon, N. J.; Noh, J. H.; Yang, W. S.; Seo, J.; Yun, J. S.; Ho-Baillie, A.; Huang, S.; Green, M. A.; Seidel, J.; Ahn, T. K.; Seok, S. I. Beneficial Effects of  $\text{PbI}_2$  Incorporated in Organo-Lead Halide Perovskite Solar Cells. *Adv. Energy Mater.* **2016**, *6*, No. 1502104.
- (32) Liu, F.; Dong, Q.; Wong, M. K.; Djurišić, A. B.; Ng, A.; Ren, Z.; Shen, Q.; Surya, C.; Chan, W. K.; Wang, J.; Ng, A. M. C.; Liao, C.; Li, H.; Shih, K.; Wei, C.; Su, H.; Dai, J. Is Excess  $\text{PbI}_2$  Beneficial for Perovskite Solar Cell Performance? *Adv. Energy Mater.* **2016**, *6*, No. 1502206.
- (33) Tauc, J. Optical Properties and Electronic Structure of Amorphous Ge and Si. *Mater. Res. Bull.* **1968**, *3*, 37–46.
- (34) Conings, B.; Babayigit, A.; Klug, M. T.; Bai, S.; Gauquelin, N.; Sakai, N.; Wang, J. T.-W.; Verbeeck, J.; Boyen, H.-G.; Snaith, H. J. A Universal Deposition Protocol for Planar Heterojunction Solar Cells with High Efficiency Based on Hybrid Lead Halide Perovskite Families. *Adv. Mater.* **2016**, *28*, 10701–10709.
- (35) Guo, F.; Yang, B.; Yuan, Y.; Xiao, Z.; Dong, Q.; Bi, Y.; Huang, J. A Nanocomposite Ultraviolet Photodetector Based on Interfacial Trap-Controlled Charge Injection. *Nat. Nanotechnol.* **2012**, *7*, 798–802.
- (36) Kim, H.-S.; Lee, C.-R.; Im, J.-H.; Lee, K.-B.; Moehl, T.; Marchioro, A.; Moon, S.-J.; Humphry-Baker, R.; Yum, J.-H.; Moser, J. E.; Grätzel, M.; Park, N.-G. Lead Iodide Perovskite Sensitized All-Solid-State Submicron Thin Film Mesoscopic Solar Cell with Efficiency Exceeding 9%. *Sci. Rep.* **2012**, *2*, No. 591.
- (37) Heo, J. H.; Im, S. H.; Noh, J. H.; Mandal, T. N.; Lim, C.-S.; Chang, J. A.; Lee, Y. H.; Kim, H.-j.; Sarkar, A.; Nazeeruddin, Md. K.; Grätzel, M.; Seok, S. I. Efficient Inorganic–Organic Hybrid Heterojunction Solar Cells Containing Perovskite Compound and Polymeric Hole Conductors. *Nat. Photonics* **2013**, *7*, 486–491.
- (38) Kim, C. S.; Lee, S. S.; Gomez, E. D.; Kim, J. B.; Loo, Y.-L. Transient Photovoltaic Behavior of Air-Stable, Inverted Organic Solar Cells with Solution-Processed Electron Transport Layer. *Appl. Phys. Lett.* **2009**, *94*, No. 113302.
- (39) Kim, J.; Kim, G.; Choi, Y.; Lee, J.; Park, S. H.; Lee, K. Light-Soaking Issue in Polymer Solar Cells: Photoinduced Energy Level Alignment at the Sol–Gel Processed Metal Oxide and Indium Tin Oxide Interface. *J. Appl. Phys.* **2012**, *111*, No. 114511.
- (40) Trost, S.; Behrendt, A.; Becker, T.; Polywka, A.; Görre, P.; Riedl, T. Tin Oxide ( $\text{SnO}_x$ ) as Universal “Light-Soaking” Free Electron Extraction Material for Organic Solar Cells. *Adv. Energy Mater.* **2015**, *5*, No. 1500277.
- (41) Yan, Y.; Cai, F.; Yang, L.; Li, J.; Zhang, Y.; Qin, F.; Xiong, C.; Zhou, Y.; Lidzey, D. G.; Wang, T. Light-Soaking-Free Inverted Polymer Solar Cells with an Efficiency of 10.5% by Compositional and Surface Modifications to a Low-Temperature-Processed  $\text{TiO}_2$  Electron-Transport Layer. *Adv. Mater.* **2017**, *29*, No. 1604044.
- (42) Lei, Y.; Zhang, L. D.; Meng, G. W.; Li, G. H.; Zhang, X. Y.; Liang, C. H.; Chen, W.; Wang, S. X. Preparation and Photoluminescence of Highly Ordered  $\text{TiO}_2$  Nanowire Arrays. *Appl. Phys. Lett.* **2001**, *78*, 1125–1127.
- (43) Chang, Y.-H.; Liu, C.-M.; Chen, C.; Cheng, H.-E. The Effect of Geometric Structure on Photoluminescence Characteristics of 1-D  $\text{TiO}_2$  Nanotubes and 2-D  $\text{TiO}_2$  Films Fabricated by Atomic Layer Deposition. *J. Electrochem. Soc.* **2012**, *159*, D401–D405.
- (44) Wu, J.-M.; Shih, H. C.; Wu, W.-T. Growth of  $\text{TiO}_2$  Nanorods by Two-Step Thermal Evaporation. *J. Vac. Sci. Technol., B: Microelectron. Nanometer Struct.—Process., Meas., Phenom.* **2005**, *23*, 2122–2126.
- (45) Sze, S. M.; Ng, K. K. *Physics of Semiconductor Devices*; John Wiley & Sons: Hoboken, NJ, 2006; pp 437–442.